

Enhancement of thermoelectric performance across the topological phase transition in dense lead selenide

HPSTAR
821-2019Liu-Cheng Chen¹, Pei-Qi Chen², Wei-Jian Li¹, Qian Zhang^{3,4}, Viktor V. Struzhkin^{1,5}, Alexander F. Goncharov⁵, Zhifeng Ren⁴ and Xiao-Jia Chen^{1*}

Alternative technologies are required in order to meet a worldwide demand for clean non-polluting energy sources. Thermoelectric generators, which generate electricity from heat in a compact and reliable manner, are potential devices for waste heat recovery. However, thermoelectric performance, as encapsulated by the figure of merit ZT, has remained at around 1.0 at room temperature, which has limited practical applications. Here, we study the effects of pressure on ZT in Cr-doped PbSe, which has a maximum ZT of less than 1.0 at a temperature of about 700 K. By applying external pressure using a diamond anvil cell, we obtained a room-temperature ZT value of about 1.7. From thermoelectric, magnetoresistance and Raman measurements, as well as density functional theory calculations, a pressure-driven topological phase transition is found to enable this enhancement. Experiments also support the appearance of a topological crystalline insulator after the transition. These findings point to the possibility of using compression to increase not just ZT in existing thermoelectric materials, but also the possibility of realizing topological crystalline insulators.

Thermoelectric (TE) materials have demonstrated great potential in enabling the conversion between thermal and electrical energy, which is especially useful in the face of the current global energy crisis^{1–3}. The critical limitation for the TE materials studied so far is their relatively low conversion efficiency, which is determined by the TE figure of merit. The figure of merit is defined as $ZT = S^2\sigma T/\kappa$, where S is the Seebeck coefficient, σ is the electrical conductivity, T is the absolute temperature and κ is the thermal conductivity. The interdependencies of S , σ and κ complicate the efforts to improve ZT. For a TE device with a Carnot efficiency of more than 15%, a TE material with an average $ZT \geq 1.5$ should be used. Such high peak ZT values have indeed been realized at high temperatures in many bulk materials^{4–10}. However, many technological applications require the operation of TE materials at room temperature. Only a few families have been reported to possess $ZT \sim 1$ close to room temperature^{4,11}. This ZT record remained unbroken for over 60 years¹².

Exploring the principle controlling ZT enhancement and searching for new materials with efficient TE performance are the two key tasks in this research field. Doping and alloying have generally been used as methods to optimize the carrier concentration in order to enhance the electrical transport properties^{1–3}. Nanostructuring can significantly reduce thermal conductivity due to the enhancement of boundary scattering⁴. This technique led to the discoveries of rather high peak ZTs of ~ 2.2 in PbTe/SrTe and $\text{AgPb}_m\text{SbTe}_{2+m}$ ^{6,7}. Similarly, ZT enhancement was found in some nanoscale materials in their superparamagnetic states due to the considerable reduction of the thermal conductivity¹³. Meanwhile, some novel approaches and materials have been developed on the basis of electronic structure manipulation, such as the electronic density distortion⁸ and the band convergence effect⁹, as well as the existence of a charge

density wave state¹⁴. The realization of high ZT in liquid-like TE materials¹⁰ is thought to result from both the optimization of the electrical transport properties and the reduction of the thermal conductivity. Pressure as a fundamental thermodynamic variable can dramatically modify the crystal, electronic and magnetic structure of a material without introducing impurities. The application of pressure has led to significant improvement of the power factor ($\text{PF} = S^2\sigma$) in many TE materials^{15,16}. With recent developments in techniques, all TE properties can now be measured at high pressures^{17,18}. Large ZT enhancement has been achieved upon compression^{17,18}. It turns out that the same maximum ZT value at high temperature in a material can be reached at room temperature solely by applying pressure¹⁸. Here we choose $\text{Pb}_{0.99}\text{Cr}_{0.01}\text{Se}$ as an example to show how pressure can be used to tune TE properties. This material has the highest TE efficiency among all of the n -type and p -type PbSe materials reported to date^{19–26}. We show that a room-temperature value of ZT increases dramatically under pressure, reaching 1.7 at a pressure of around 3 GPa. This is high for an operating temperature of 300 K when compared to all of the TE materials studied so far^{1–3}. Furthermore, we achieve a topological crystalline insulator (TCI) at higher pressures, which was theoretically predicted in such a material class^{27–29}.

Results

TE properties at ambient pressure. In order to establish the baseline for the TE properties of $\text{Pb}_{0.99}\text{Cr}_{0.01}\text{Se}$ at high pressures, we began by measuring the electrical and thermal transport properties from 2 to 300 K at ambient pressure. The results are shown in Supplementary Fig. 1. The data at high temperatures were taken from earlier measurements of the same sample²⁶. Good agreement can be seen between the low- and high-temperature regimes.

¹Center for High Pressure Science and Technology Advanced Research, Shanghai, China. ²Massachusetts Institute of Technology, Cambridge, MA, USA.

³Department of Materials Science and Engineering, Harbin Institute of Technology, Shenzhen, Guangdong, China. ⁴Department of Physics and TcSUH,

University of Houston, Houston, TX, USA. ⁵Geophysical Laboratory, Carnegie Institution of Washington, Washington DC, USA. *e-mail: xjchen@hpstar.ac.cn

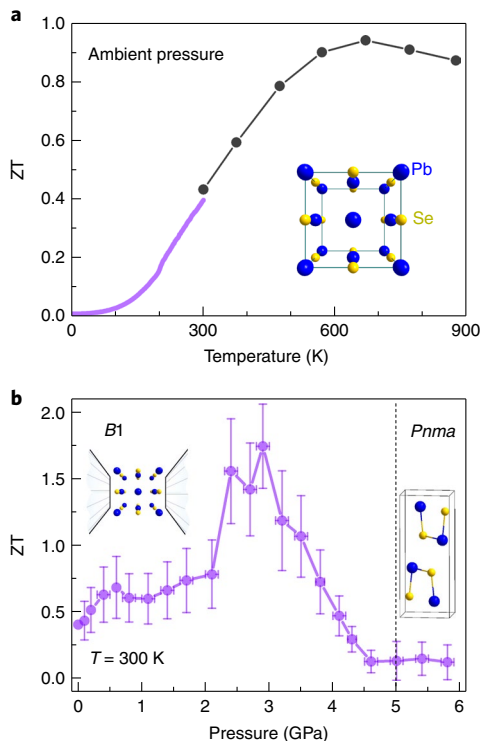


Fig. 1 | The dimensionless figure of merit ZT of $Pb_{0.99}Cr_{0.01}Se$.

a, Temperature dependence of ZT at ambient pressure. The ZT values at low temperatures were obtained by using PPMS, and the data at high temperatures were taken from an earlier study on the same sample²⁶. The inset illustrates the crystal structure of the sample in the $B1$ phase. **b**, Pressure-dependent ZT at 300 K. The errors for ZT are given for the uncertainties in the measurements of the resistivity, Seebeck coefficient and thermal conductivity. The structures for the $B1$ and $Pnma$ phases are shown in the insets for the low-pressure and high-pressure regions, respectively. The dashed line indicates the beginning of the $Pnma$ phase.

The minor deviations of the studied TE parameters near 300 K arise mainly from small systematic errors in the two experiments. Although PbSe has a very small direct band gap¹⁹, σ of $Pb_{0.99}Cr_{0.01}Se$ decreases sharply upon cooling at low temperatures and then saturates with further decreasing temperature, exhibiting a semiconducting behaviour. In addition, the negative value of S continuously decreases with increasing temperature, indicating an n -type degenerate semiconducting character. The temperature dependence of κ has a typical λ shape, increasing sharply as T^{-3} and then decreasing as T^{-1} with increasing temperature after passing the maximum value. Generally, this typical behaviour of κ is controlled by grain boundary scattering and three-phonon scattering via Umklapp processes¹⁻³. The power factor PF is also shown in Supplementary Fig. 1. The maximum value of PF is about $30 \mu W cm^{-1} K^{-2}$ at 300 K. Such a maximum provides a good starting point for our study focusing on the TE performance at 300 K.

Figure 1a,b shows the temperature-dependent ZT at ambient pressure and the pressure-dependent ZT at 300 K, respectively. As observed, the ZT values at low temperatures agree well with another set of data at high temperatures (Fig. 1a), as a result of the parameters σ , S , κ and PF being self-consistent over the whole temperature range (Supplementary Fig. 1). The Cr-doped PbSe shares the same structure with its parent compound at ambient pressure (the $B1$ phase, shown in the inset of Fig. 1a). With increasing temperature, ZT monotonically increases until it reaches a maximum value (less than 1) near 700 K and then it decreases at higher temperatures.

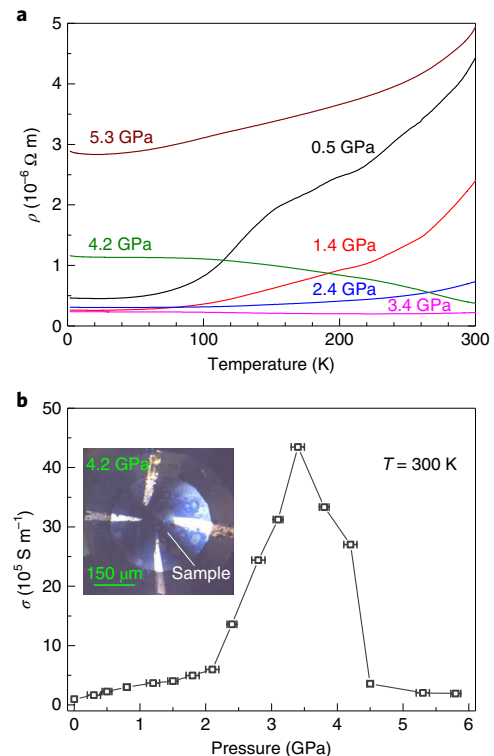


Fig. 2 | The electrical resistivity and conductivity of $Pb_{0.99}Cr_{0.01}Se$ at high pressures.

a, Temperature dependence of the resistivity ρ at various pressures up to 5.3 GPa. **b**, Pressure dependence of the electrical conductivity σ at 300 K. The error bars correspond to the uncertainties of the measured data. The inset shows the geometry of the electrical transport measurements at a pressure of 4.2 GPa. Four Pt wires were attached to the sample.

With increasing pressure, ZT first monotonically increases until 2 GPa and then it jumps up and reaches a maximum value of ~ 1.7 at about 2.8 GPa (Fig. 1b). It then continuously decreases until 4.5 GPa before finally maintaining a nearly constant value until near 6 GPa.

Evolution of the structural properties with pressure. From the high-pressure X-ray diffraction data, we can find that all of the Bragg peaks of $Pb_{0.99}Cr_{0.01}Se$ shift monotonically to higher angles with increasing pressure, indicating the shrinkage of the lattice (Supplementary Fig. 2). New peaks emerge when pressure is increased to 5.5 GPa, indicating the phase transition from $B1$ to $Pnma$ (Supplementary Fig. 2 and Supplementary Note 1). The lattice parameters obtained for these two phases are shown in Supplementary Fig. 2. The two phases coexist in the pressure range from 5.5 to 8.5 GPa. The same behaviour is also detected from Raman scattering measurements (Supplementary Fig. 3 and Supplementary Note 2). The significant enhancement of the ZT value obtained is in the $B1$ phase.

Effect of pressure on the resistivity. The detailed results of the resistivity ρ of $Pb_{0.99}Cr_{0.01}Se$ as a function of temperature for selected pressures are summarized in Fig. 2. As can be seen, the temperature-dependent ρ is strongly suppressed by increasing pressure up to 3.4 GPa and shows a metallic behaviour. Upon further compression, ρ has a sudden increase and is characterized by a non-metallic feature at a pressure of 4.2 GPa (Fig. 2a). The room-temperature electrical conductivity σ at various pressures was extracted from the temperature dependences and the results are illustrated in Fig. 2b. Compared with the ambient pressure value, the room-temperature

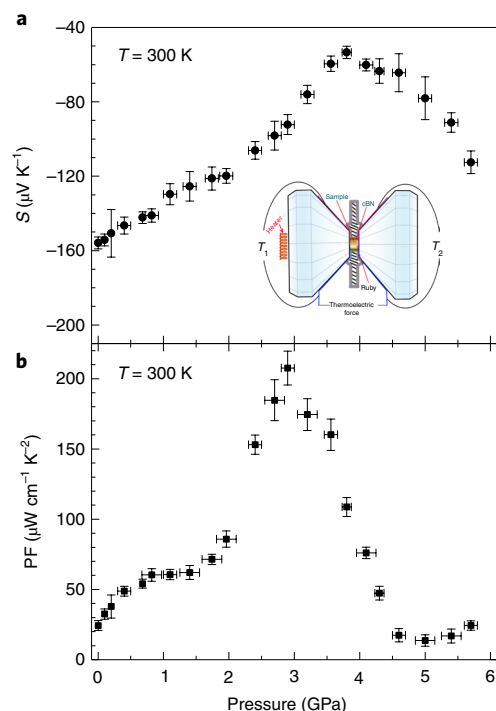


Fig. 3 | The Seebeck coefficient and power factor of $\text{Pb}_{0.99}\text{Cr}_{0.01}\text{Se}$ at high pressures. **a**, Pressure dependence of the Seebeck coefficient S at 300 K. The inset shows the diagram of Seebeck coefficient measurements under pressure. The sample was placed in the chamber, which was surrounded by cubic boron nitride as insulating layers. Ruby was used to determine the pressure. The error bars are the standard deviations from the fitted results to the experimental data. T_1 and T_2 represent the temperatures of each side of the sample. **b**, Pressure dependence of the power factor PF at 300 K. The error bars correspond to the uncertainties of all the related experimental data.

σ increases significantly with increasing pressure and reaches a maximum value ($\sim 44 \times 10^3 \text{ S m}^{-1}$) at about 3.4 GPa. Then σ drops sharply with further increasing pressure up to 4.5 GPa. Upon heavy compression to near 6 GPa, σ has only a small additional dip, which may be due to the appearance of the more stable $Pnma$ structure (Supplementary Fig. 2). Our high-pressure resistivity data are similar to the previous reports for undoped material¹⁶. The sharp increase of σ between 2 and 3.5 GPa does not originate from a structural transition (Supplementary Figs. 2 and 3). The emergence of the sharply increased σ is probably controlled by the electronic structure, which is tuned by pressure. We assign the σ behaviour to the pressure-driven topological phase transition (TPT)^{30,31}, as detailed in the ‘Pressure-induced TPT and TCI’ section, based on our observations and calculations.

Pressure dependence of the Seebeck coefficient. The high-pressure Seebeck coefficient S was determined based on a technique developed recently^{17,18}. The details are given in the Methods and Supplementary Fig. 4. The pressure dependence of S for $\text{Pb}_{0.99}\text{Cr}_{0.01}\text{Se}$ at 300 K is summarized in Fig. 3a. The results are similar to previous reports on undoped PbSe ¹⁶. In the pressure range studied, all of the S values are negative, indicating the electron doping feature by introducing Cr. The absolute value of S decreases with increasing pressure until reaching a dip at around 3.8 GPa before climbing up again at higher pressures. The asymmetrical form of S with external pressure is the typical feature expected in the vicinity of the TPT^{30,31}. Since S is the derivative of the density of states at the Fermi level, it is strongly affected by the TPT³⁰. Raman scattering data provide spectroscopic evidence for this interesting phenomenon in the studied

material (Supplementary Note 3 and Supplementary Figs. 3 and 5). Moreover, the TPT scenario also offers a natural explanation for the observed bell shape of the pressure dependence of σ (Fig. 2). Here pressure serves as an external parameter that tunes the system.

Pressure effect on the power factor. By combining σ and S , one can obtain PF for $\text{Pb}_{0.99}\text{Cr}_{0.01}\text{Se}$ at high pressures. The results are shown in Fig. 3b. It can be seen that the PF value clearly increases with increasing pressure in the vicinity of critical pressure P_c around 3 GPa, and then decreases rapidly after passing the maximum value of $210 \mu\text{W cm}^{-1} \text{ K}^{-2}$. This maximum PF is almost one order of magnitude higher than those values found from doping either by electrons^{20,21,24–26} or holes^{22,23}. A summary of the maximum values of the PF of the n -type PbSe materials at the corresponding temperature is given in Supplementary Table 1. The significant improvement of the PF under pressure is mainly attributed to the sharply increased σ values without a substantial reduction of S . Both the bell shape of σ and the asymmetrical form of S indicate the pressure-driven TPT. They together contribute to the bell shape of the PF.

Hall effect under pressure. To further understand the obtained electrical transport properties, we also performed high-pressure Hall effect measurements. The carrier mobility (μ) of the bulk material can be calculated from the measured Hall resistance and σ . The obtained μ and the carrier concentration n_H as a function of pressure for $\text{Pb}_{0.99}\text{Cr}_{0.01}\text{Se}$ at 300 K are shown in Supplementary Fig. 6. The negative sign of n_H confirms the electron doping by Cr. At ambient pressure, n_H has a nearly optimal absolute value of $\sim 1 \times 10^{19} \text{ cm}^{-3}$, indicating the excellent TE performance of this material even at ambient pressure. The absolute value of n_H increases monotonically with increasing pressure to $3 \times 10^{19} \text{ cm}^{-3}$ at 4.2 GPa. It then has a sudden decrease upon further compression (Supplementary Fig. 6a). However, the mobility μ exhibits a peak at around 3 GPa (Supplementary Fig. 6b). Therefore, we attribute the significant increase of the PF value of $\text{Pb}_{0.99}\text{Cr}_{0.01}\text{Se}$ to TPT. These results show that applying pressure to drive a system across the TPT is indeed an efficient means to improve the PF of TE materials.

Pressure-induced TPT and TCI. Band inversion in the bulk insulating electronic structure is the key requirement for the appearance of metallic surface states in TCIs with crystal symmetry²⁷. For the face-centred-cubic Brillouin zone (Fig. 4a), the (111) plane containing the high-symmetry points Γ , L, U and X is chosen to show pressure-induced band inversion and TPT. The results are presented in Fig. 4b,c. The projected (001) surface containing $\bar{\Gamma}$, \bar{X} and \bar{M} is chosen to show the formation of the surface states for TCI after the TPT (Fig. 4d). The calculated band structure for PbSe reveals pressure-driven band inversion (Fig. 4b and Supplementary Fig. 7). The band gap near the high-symmetry point L in the Brillouin zone is found to narrow down upon compression and close at 2.6 GPa, and then reopen afterward with an inversion between the conduction band and the valence band³². The TPT is accompanied by this inversion process (Fig. 4c). From the top view over the (111) plane, the small pockets represent available electronic states close at the top of the valence band. The pockets outside of the hexagon centre are located at the L point, and the pockets inside the hexagon are located at the Γ –U line. At ambient pressure, the centre pocket is located at the Γ –L line. At 2.6 GPa, the centre pocket located on the Γ –L lines disappears, which is a characteristic of the TPT. When the bulk band gap reopens, the material enters a TCI state featuring metallic properties at the surface but insulating ones in the bulk (Fig. 4d).

The linear magnetoresistance at low magnetic fields is a hallmark for topological insulators³³. We do detect such a feature when the material passes the TPT, for example for the linear magnetoresistivity at a pressure of 4.2 GPa and a low temperature of 15 K. This is different to the nearly parabolic magnetic field dependence of

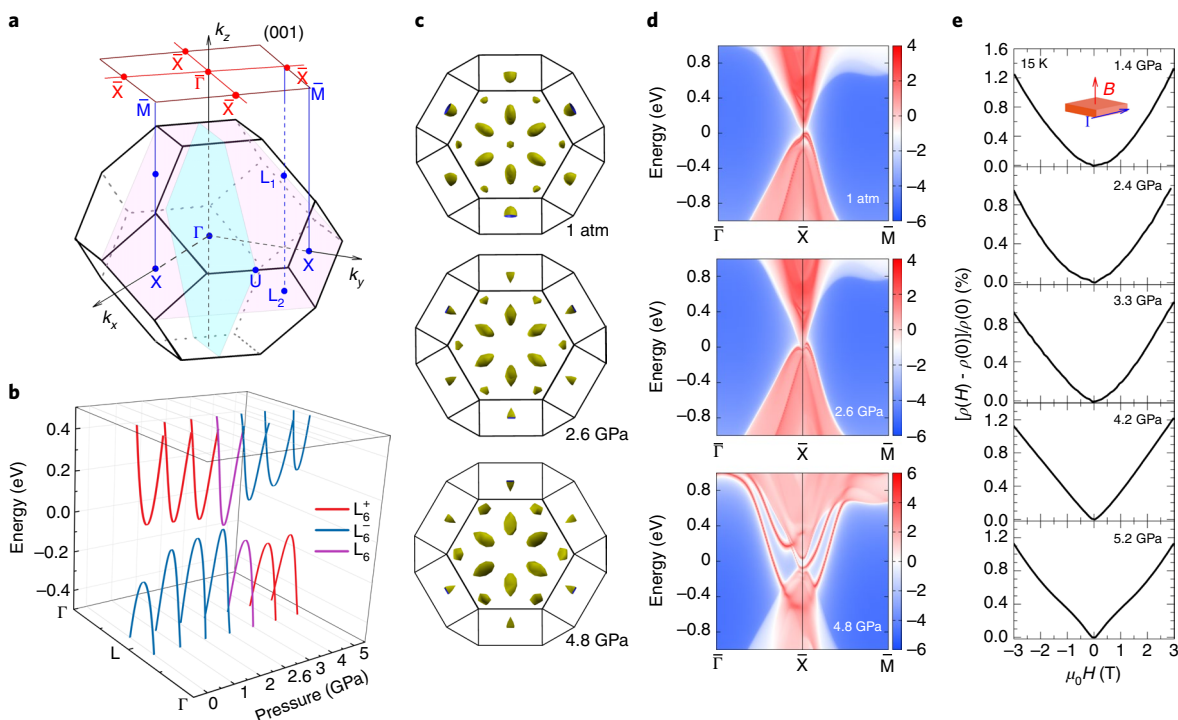


Fig. 4 | Band structure and TCI state in $\text{Pb}_{0.99}\text{Cr}_{0.01}\text{Se}$ under pressure. **a**, The face-centred-cubic Brillouin zone. The colour (111) plane containing the high-symmetry points Γ , L, U and X is chosen to show pressure-induced band inversion and TPT. The projection onto the (001) surface containing $\bar{\Gamma}$, \bar{X} and \bar{M} is used to show the formation of the surface states for TCI after the TPT. Here, $\mathbf{k} = (k_x, k_y, k_z)$ is the wavevector in momentum space. **b**, Evolution of the band gap near the high-symmetry point L for PbSe with pressure. The valence- and conduction-band edges occur at the L point in an L_6^+ state and an L_6^- state, respectively. The application of pressure leads to the energy gap shrinkage as the L_6^+ and L_6^- states approach each other, closure to nearly zero at a critical pressure of 2.6 GPa where the two states become degenerate and then reopening with the L_6^+ state now forming the conduction-band edge and the L_6^- state forming the valence-band edge. **c**, Top view over the (111) plane at selected pressures to show the TPT character. The small pockets represent available electronic states close at the top of the valence band. The pockets outside of the hexagon centre are located at the L point and the pockets inside the hexagon are located at the Γ –U line. **d**, Energy and momentum dispersion with the local density of states on the (001) surface at ambient pressure, 2.6 GPa and 4.8 GPa (from top to bottom). The surface states can be observed around the \bar{X} point with the reopened band gap for the bulk. Here, the warmer colours correspond to the higher local densities of states. The red regions indicate the bulk energy bands and the blue regions indicate the bulk energy gaps. A non-trivial TCI phase is formed after passing 2.6 GPa. **e**, The magnetoresistivity $[\rho(H) - \rho(0)]/\rho(0)$ taken at a temperature of 15 K for selected pressures as a function of the magnetic field H . The directions for the applied magnetic field and current on the sample are shown in the inset.

the magnetoresistivity for pressures below P_c for the TPT (Fig. 4e). The linear magnetoresistivity provides direct transport evidence for the experimental realization of the TCI state in this material. The cone shape of the magnetoresistivity versus magnetic field is also observed for higher pressures far beyond the TPT (the case for 5.2 GPa in Fig. 4e). This behaviour probably results from a collective effect of the weak antilocalization of the surface bands and the weak localization of the bulk bands in topological insulators³⁴. The enhanced weak localization effect from the bulk bands for pressures far beyond the TPT is due to the reopened band gap at such higher pressures (Fig. 4b). These magnetoresistivity results are in excellent agreement with the features for the TPT and TCI as indicated in Fig. 4b–d. This is further supported by the observed pressure-dependent behaviours of ρ and S , the maxima in the linewidths of two major Raman-active phonon modes and the minima of the difference in their frequencies (Supplementary Fig. 3 and 5). The experimental realization of the TCI state in $\text{Pb}_{0.99}\text{Cr}_{0.01}\text{Se}$ solely through pressure^{28,29} is another central finding of this work.

Pressure effects on the thermal conductivity and figure of merit.

For exploring TE performance, we carried out high-pressure κ measurements by using our previously developed technique^{17,18}. The details are given in the Methods and Supplementary Note 4 together with Supplementary Figs. 8 and 9. The obtained κ for $\text{Pb}_{0.99}\text{Cr}_{0.01}\text{Se}$ increases by approximately a factor of four with the

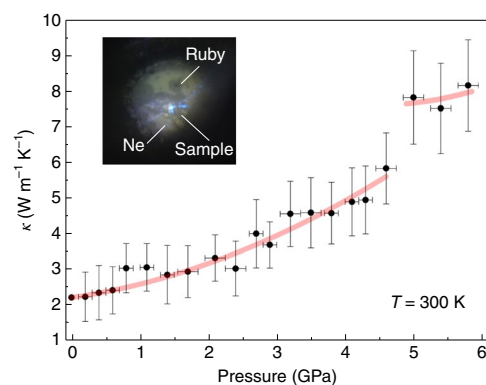


Fig. 5 | The thermal conductivity of $\text{Pb}_{0.99}\text{Cr}_{0.01}\text{Se}$ at high pressures.

The values of κ were obtained at each pressure of interest and at 300 K. The lines are guides for the eye. This discontinuity of the data points and the curves indicates the structural transition. The error bars are the uncertainties of the first-order temperature (laser power) derivatives of the phonon frequencies. The inset shows the microscopic photograph for the measurements of the thermal conductivity under pressure. The ruby near the sample was used to determine pressure. Neon was loaded to serve as the pressure-transmitting medium. The details of the measurements are given in the Supplementary Information.

application of pressure up to 4.8 GPa (Fig. 5). The obtained large Grüneisen parameters are a good indicator for a low heat conduction in this material in the B1 phase (Supplementary Note 5). When the *Pnma* phase is evident, κ jumps up to a larger value. In the B1 phase, the obtained pressure dependences of σ and the full width at half maximum of the phonon mode can be used to provide the quantitative estimation of the electronic and lattice contributions to κ (Supplementary Note 6). As can be seen from Supplementary Fig. 10, the lattice component of κ behaves similarly to the total κ except for the slight decline in the vicinity of P_c for the TPT. Meanwhile, the electronic component of κ exhibits an asymmetrical shape with a maximum at ~ 3.7 GPa. As a result, both the lattice and electrons jointly conduct heat at high pressures. The high-pressure thermal conductivity is also strongly affected by the TPT in this material. The pressure-dependent ZT of $\text{Pb}_{0.99}\text{Cr}_{0.01}\text{Se}$ at 300 K was thus determined for each pressure based on the obtained σ , S and κ values (Fig. 1b). It is apparent that the pressure-induced increase of κ is not a favourable factor for ZT. The significant enhancement of ZT with pressure results from the increase of PF through the large improvement of σ due to the pressure-driven TPT.

We found an enhanced room-temperature ZT in $\text{Pb}_{0.99}\text{Cr}_{0.01}\text{Se}$ at P_c of around 3 GPa, followed by the entrance to a TCI phase. A pressure-driven TPT is believed to account for such an enhancement. The supporting σ and S data (Supplementary Fig. 11) and Raman spectroscopy results (Supplementary Fig. 3) are reproducible in a number of independent experimental runs. Even though the results scatter for PF and thus for ZT, the pressure-dependent ZT with maximum value above 1 is robust for this material even when averaging all of the available data (Supplementary Fig. 11). The present study thus offers a new direction to further improve the TE performance of existing TE materials simply through lattice compression or other equivalent methods that can be used to tune the material to the TPT conditions.

Instead of reaching the optimal conditions for the enhanced ZT by compression, one can explore the possibility of chemical doping, which would shrink the lattice. An excellent example along this direction was that the discovery of the first cuprate superconductor with a critical temperature above liquid nitrogen temperature was triggered by the observed strong pressure effect in the La–Ba–Cu–O system³⁵. Whether similar enhancement in the ZT of TE materials can be realized through lattice shrinkage at ambient pressure remains to be seen and deserves further study. However, this idea has been realized already by creating TCI states in $\text{Pb}_{1-x}\text{Sn}_x\text{Se}$ ³⁶ and $\text{Pb}_{1-x}\text{Sn}_x\text{Te}$ ³⁷. Doping Sn in both ternary alloys to reduce crystal volume is thus expected to result in excellent TE performance due to the gap closure and occurrence of TPT at certain temperatures^{36–38}.

Online content

Any methods, additional references, Nature Research reporting summaries, source data, statements of code and data availability and associated accession codes are available at <https://doi.org/10.1038/s41563-019-0499-9>.

Received: 8 November 2018; Accepted: 3 September 2019;

Published online: 07 October 2019

References

- Chen, G., Dresselhaus, M. S., Dresselhaus, G., Fleurial, J. P. & Cailla, T. Recent developments in thermoelectric materials. *Int. Mater. Rev.* **48**, 45–66 (2003).
- Snyder, G. J. & Toberer, E. S. Complex thermoelectric materials. *Nat. Mater.* **7**, 105–144 (2008).
- Ren, Z. F., Lan, Y. C. & Zhang, Q. Y. *Advanced Thermoelectrics: Materials, Contacts, Devices, and System* (CRC Press, 2017).
- Poudel, B. et al. High-thermoelectric performance of nanostructured bismuth antimony telluride bulk alloys. *Science* **320**, 634–638 (2008).
- Pei, Y. Z., Heinz, N. A., LaLonde, A. & Snyder, G. J. Combination of large nanostructures and complex band structure for high performance thermoelectric lead telluride. *Energy Environ. Sci.* **4**, 3640–3645 (2011).
- Biswas, K. et al. High-performance bulk thermoelectrics with all-scale hierarchical architectures. *Nature* **489**, 414–418 (2012).
- Hsu, K. F. et al. Cubic $\text{AgPb}_m\text{SbTe}_{2+m}$: bulk thermoelectric materials with high figure of merit. *Science* **303**, 818–821 (2004).
- Heremans, J. P. et al. Enhancement of thermoelectric efficiency in PbTe by distortion of the electronic density of states. *Science* **321**, 554–557 (2008).
- Pei, Y. Z. et al. Convergence of electronic bands for high performance bulk thermoelectrics. *Nature* **473**, 66–69 (2011).
- Liu, H. et al. Copper ion liquid-like thermoelectrics. *Nat. Mater.* **11**, 422–425 (2012).
- Zhu, T. J. et al. Hot deformation induced bulk nanostructuring of unidirectionally grown *p*-type $(\text{Bi,Sb})_2\text{Te}_3$ thermoelectric materials. *J. Mater. Chem. A* **1**, 11589–11594 (2013).
- Wright, D. A. Thermoelectric properties of bismuth telluride and its alloys. *Nature* **181**, 834–834 (1958).
- Zhao, W. et al. Superparamagnetic enhancement of thermoelectric performance. *Nature* **549**, 247–251 (2017).
- Rhyee, J. S. et al. Peierls distortion as a route to high thermoelectric performance in $\text{In}_2\text{Se}_{3-\delta}$ crystals. *Nature* **459**, 965–968 (2009).
- Polvani, D. A., Meng, J. F., Chandra Shekar, N. V., Sharp, J. & Badding, J. V. Large improvement in thermoelectric properties in pressure-tuned *p*-type $\text{Sb}_{1.5}\text{Bi}_{0.5}\text{Te}_3$. *Chem. Mater.* **13**, 2068–2071 (2001).
- Shchennikov, V. V., Ovsyannikov, S. V. & Derevskov, A. Y. Thermopower of lead chalcogenides at high pressures. *Phys. Solid State* **44**, 1845–1849 (2002).
- Yu, H. et al. Impressive enhancement of thermoelectric performance in CuInTe , upon compression. *Mater. Today Phys.* **5**, 1–5 (2018).
- Chen, L. C. et al. Pressure-induced enhancement of thermoelectric performance in palladium sulfide. *Mater. Today Phys.* **5**, 64–71 (2018).
- Parker, D. & Singh, D. J. High-temperature thermoelectric performance of heavily doped PbSe. *Phys. Rev. B* **82**, 035204 (2010).
- Androulakis, J. et al. High-temperature thermoelectric properties of *n*-type PbSe doped with Ga, In, and Pb. *Phys. Rev. B* **83**, 195209 (2011).
- Lee, Y. et al. Contrasting role of antimony and bismuth dopants on the thermoelectric performance of lead selenide. *Nat. Commun.* **5**, 3640 (2014).
- Wang, H., Pei, Y. Z., LaLonde, A. D. & Snyder, G. J. Heavily doped *p*-type PbSe with high thermoelectric performance: an alternative for PbTe. *Adv. Mater.* **23**, 1366–1370 (2011).
- Wang, H., Gibbs, Z. M., Takagiwa, Y. & Snyder, G. J. Tuning bands of PbSe for better thermoelectric efficiency. *Energy Environ. Sci.* **7**, 804–811 (2014).
- Zhang, Q. et al. Study of the thermoelectric properties of lead selenide doped with boron, gallium, indium, or thallium. *J. Am. Chem. Soc.* **134**, 17731–17738 (2012).
- Zhang, Q. Y. et al. Enhancement of thermoelectric figure-of-merit by resonant states of aluminium doping in lead selenide. *Energy Environ. Sci.* **5**, 5246–5251 (2012).
- Zhang, Q. et al. Enhancement of thermoelectric performance of *n*-type PbSe by Cr doping with optimized carrier concentration. *Adv. Energy Mater.* **5**, 1401977 (2015).
- Fu, L. Topological crystalline insulators. *Phys. Rev. Lett.* **106**, 106802 (2011).
- Hsieh, T. H. et al. Topological crystalline insulators in the SnTe material class. *Nat. Commun.* **3**, 982 (2012).
- Barone, P. et al. Pressure-induced topological phase transitions in rocksalt chalcogenides. *Phys. Rev. B* **88**, 045207 (2013).
- Abrikosov, A. A. *Fundamentals of the Theory of Metals* (North-Holland, 1988).
- Blanter, Ya. M., Kaganov, M. I., Pantsulaya, A. V. & Varlamov, A. A. The theory of electronic topological transitions. *Phys. Rep.* **245**, 159–257 (1994).
- Svane, A. et al. Quasiparticle self-consistent GW calculations for PbS, PbSe, and PbTe: band structure and pressure coefficients. *Phys. Rev. B* **81**, 245120 (2010).
- Qu, D. X., Hor, Y. S., Xiong, J., Cava, R. J. & Ong, N. P. Quantum oscillations and Hall anomaly of surface states in the topological insulator Bi_2Te_3 . *Science* **329**, 821–824 (2010).
- Lu, H. Z. & Shen, S. Q. Weak localization of bulk channels in topological insulator thin films. *Phys. Rev. B* **84**, 125134 (2011).
- Wu, M. K. et al. Superconductivity at 93 K in a new mixed-phase Y–Ba–Cu–O compound system at ambient pressure. *Phys. Rev. Lett.* **58**, 908–910 (1987).
- Dziawa, P. et al. Topological crystalline insulator states in $\text{Pb}_{1-x}\text{Sn}_x\text{Se}$. *Nat. Mater.* **11**, 1023–1027 (2012).
- Xu, S. Y. et al. Observation of a topological crystalline insulator phase and topological phase transition in $\text{Pb}_{1-x}\text{Sn}_x\text{Te}$. *Nat. Commun.* **3**, 1192 (2012).
- Dimmock, J. O., Melngailis, I. & Strauss, A. J. Band structure and laser action in $\text{Pb}_x\text{Sn}_{1-x}\text{Te}$. *Phys. Rev. Lett.* **16**, 1193–1196 (1966).

Acknowledgements

The work at HPSTAR was supported by the National Key R&D Programme of China (grant no. 2018YFA0305900). The work performed at the University of Houston was funded by the Department of Energy's Basic Energy Science programme under grant no. DE-SC0010831. The work at Carnegie was funded by the US National Science Foundation under grant no. EAR-1763287. P.Q.C. acknowledges the internship programme at Carnegie Institution of Washington.

Author contributions

X.J.C. conceived the project. X.J.C. and Z.R. designed the project. Q.Z. and Z.R. synthesized the samples. L.C.C. and V.V.S. performed high-pressure X-ray diffraction measurements. P.Q.C. and A.F.G. performed high-pressure Raman spectroscopy measurements. L.C.C. and X.J.C. performed the TE properties measurements. W.J.L. and X.J.C. carried out the density functional theory calculations. All of the authors analysed

the data and discussed the underlying physics. X.J.C. wrote the paper with contributions from the other authors. The manuscript reflects the contributions of all authors.

Competing interests

The authors declare no competing interests.

Additional information

Supplementary information is available for this paper at <https://doi.org/10.1038/s41563-019-0499-9>.

Correspondence and requests for materials should be addressed to X.-J.C.

Reprints and permissions information is available at www.nature.com/reprints.

Publisher's note Springer Nature remains neutral with regard to jurisdictional claims in published maps and institutional affiliations.

© The Author(s), under exclusive licence to Springer Nature Limited 2019

Methods

Ambient-pressure TE property characterization. The studied Cr-doped PbSe samples were prepared by melting, hand milling and hot pressing. The detailed synthetic procedure for this high-quality sample is provided in a previous report²⁶. The low-temperature TE parameters (S , σ and κ) at ambient pressure were measured in a thermal transport option setup using a Physical Properties Measurement System (PPMS) by Quantum Design. The high-temperature data for the TE parameters of $\text{Pb}_{0.99}\text{Cr}_{0.01}\text{Se}$ at ambient pressure were taken from a previous work²⁶.

High-pressure resistivity, magnetoresistivity and Hall coefficient measurements.

For the high-pressure resistivity, magnetoresistivity and Hall coefficient measurements, a non-magnetic diamond anvil cell (DAC) made of Cu–Be alloy was used for PPMS³⁹. This customized cell had two symmetrical diamond anvils and the diameter of the anvil culets was 300 μm . A steel flake (T301) was used as a gasket with a sample chamber of 150 μm diameter. The gasket was insulated with cubic boron nitride and silver epoxy. A cut piece of the polycrystalline sample was placed into the sample chamber. Four Pt wires were placed on the surface of one side of the insulated gasket with the linkage of the sample and the external Cu wires. A standard four-probe method was used for the electrical transport measurements. The resistivity and Hall coefficient were determined in terms of the van der Pauw method⁴⁰. For this method, the thickness of the measured sample is the only needed dimensional parameter.

High-pressure Seebeck coefficient measurements. High-pressure Seebeck coefficient measurements were based on the definition $S = \Delta V / \Delta T$ by using the technique described recently^{17,18}. The detailed setup diagram is shown in the inset of Fig. 3a. The temperature gradient (ΔT) between the two sides of the sample was generated by an external heater attached to one side of the diamond. The ΔT was measured by two separate W–Ta thin thermocouples connected to two digital temperature controllers. At the same time, the TE voltage (ΔV) along the temperature gradient was read out by a digital multimeter (218-A-5900, Keithley) within the same thermocouple material. The representative TE voltage (ΔV) and temperature gradient (ΔT) at pressures of interest are shown in Supplementary Fig. 4. The S values were obtained by fitting the slopes of $\Delta V / \Delta T$.

High-pressure thermal conductivity measurements. The details of the κ measurements have been described in our previous studies^{17,18}. The optical micrograph of the κ measurements inside the DAC is shown in the inset of Fig. 5. Pressure was created by using a symmetrical DAC with two 300 μm culets. A hole with a diameter of 150 μm was created in a gasket (T301). A small piece of the sample, together with a small ruby ball, was loaded into the sample chamber. The pressure-transmitting medium in the sample chamber was neon. The temperature of the sample chamber was controlled by an internal heater surrounding the gasket. The Raman signal of the sample was collected by a charge-coupled device. The wavelength of the exciting laser for the Raman system was 488 nm. The scattered light was focused on an 1,800 gmm^{-1} grating in order to obtain better Raman scattering spectra.

High-pressure X-ray diffraction measurements. For the synchrotron structural study, the X-ray diffraction patterns were collected at the Advanced Photon Source of Argonne National Laboratory, USA. A wavelength of 0.3100 \AA and a size of the focus beam of less than 2 μm were chosen for the measurements. The prepared DAC was the same as that used in the Raman scattering measurements. The sample was pressed into powders before being placed into the chamber. The obtained two-dimensional X-ray diffraction patterns were integrated into one-dimensional patterns with the help of the Fit2D software⁴¹. The integrated intensity versus 2θ diffraction patterns were analysed by using GSAS software⁴². For all of the experiments mentioned above, the pressure was calibrated by using the ruby fluorescence shift⁴³ and implemented at room temperature.

High-pressure Raman scattering measurements. Raman spectra were measured using a single stage spectrograph equipped with a thermoelectrically cooled charge-coupled device. The Raman notch filters were of a very narrow bandpass, allowing Raman measurements down to 10 cm^{-1} in the Stokes and anti-Stokes spectroscopy. The 488 nm excitation incidents were used to illuminate an approximately $50 \times 50 \mu\text{m}^2$ spot on the surface of the sample. The excitation strength was monitored by using a power meter.

Band-structure calculations. All the calculations were performed in the framework of density functional theory^{44,45} combined with the G_0W_0

approximations (G_0 is a non-interacting Green's function and W_0 is a screened Coulomb interaction in the frequency domain)⁴⁶, as implemented in the Vienna ab initio simulation package^{47–49}. For self-consistent field calculations, the Perdew–Burke–Ernzerhof-type generalized gradient approximation⁵⁰ was used and the plane-wave basis expansion was set to 500 eV, with a k -point grid taken as $8 \times 8 \times 8$. The band gap near the high-symmetry point L in the Brillouin zone at different pressures for PbSe is shown in Fig. 4b. The band structure in the wide range at ambient pressure is shown in Supplementary Fig. 7. The isoenergetic surface close to the top of the valence band for the selected pressures is shown in Fig. 4c. To calculate the surface states, we first constructed the maximally localized Wannier functions by using the Wannier90 package^{51–53}. The surface local density of states was calculated by employing the WannierTools package⁵⁴ using the maximally localized Wannier functions obtained. The results on the (001) surface for PbSe at selected pressures is shown in Fig. 4d. The spin–orbit coupling was included during the whole calculations. In all these calculations, the experimentally obtained equation of states for $\text{Pb}_{0.99}\text{Cr}_{0.01}\text{Se}$ was used to simulate the Cr-doping effects on PbSe.

Data availability

The data that support the findings of this study are available from the corresponding author upon reasonable request.

Code availability

All the codes created for the analysis of the data are from the open-source software packages which are cited in the references of this paper.

References

- Gavriliuk, A. G., Mironovich, A. A. & Struzhkin, V. V. Miniature diamond anvil cell for broad range of high pressure measurements. *Rev. Sci. Instrum.* **80**, 043906 (2009).
- Van der Pauw, L. J. A method of measuring specific resistivity and Hall effect of discs of arbitrary shape. *Philips Res. Repts.* **13**, 1–9 (1958).
- Hammersley, A. P., Svensson, S. O., Hanfland, M., Fitch, A. N. & Hausermann, D. Two-dimensional detector software: from real detector to idealised image or two-theta scan. *High. Press. Res.* **14**, 235–248 (1996).
- Toby, B. H. E. X. P. G. U. I. a graphical user interface for GSAS. *J. Appl. Cryst.* **34**, 210–213 (2001).
- Mao, H. K., Bell, P. M., Shaner, J. W. & Stembey, D. J. Specific volume measurements of Cu, Mo, Pd, and Ag and calibration of the ruby R_1 fluorescence pressure gauge from 0.06 to 1 Mbar. *J. Appl. Phys.* **49**, 3276–3283 (1978).
- Hohenberg, P. & Kohn, W. Inhomogeneous electron gas. *Phys. Rev. B* **136**, 864–871 (1964).
- Kohn, W. & Sham, L. J. Self-consistent equations including exchange and correlation effects. *Phys. Rev. A* **140**, 1133–1138 (1965).
- Hybertsen, M. S. & Louie, S. G. Electron correlation in semiconductors and insulators: band gaps and quasiparticle energies. *Phys. Rev. B* **34**, 5390–5413 (1986).
- Kresse, G. & Hafne, J. Ab initio molecular dynamics for liquid metals. *Phys. Rev. B* **47**, 558(R)–561(R) (1993).
- Kresse, G. & Hafner, J. Ab initio molecular-dynamics simulation of the liquid-metal amorphous-semiconductor transition in germanium. *Phys. Rev. B* **49**, 14251–14269 (1994).
- Kresse, G. & Furthmüller, J. Efficient iterative schemes for ab initio total-energy calculations using a plane-wave basis set. *Phys. Rev. B* **54**, 11169–11186 (1996).
- Perdew, J. P., Burke, K. & Ernzerhof, M. Generalized gradient approximation made simple. *Phys. Rev. Lett.* **77**, 3865–3868 (1996).
- Mostofi, A. A. et al. An updated version of Wannier90: a tool for obtaining maximally-localised Wannier functions. *Comput. Phys. Commun.* **185**, 2309–2310 (2014).
- Souza, I., Marzari, N. & Vanderbilt, D. Maximally localized Wannier functions for entangled energy bands. *Phys. Rev. B* **65**, 035109 (2001).
- Marzari, N. & Vanderbilt, D. Maximally localized generalized Wannier functions for composite energy bands. *Phys. Rev. B* **56**, 12847–12865 (1997).
- Wu, Q. S., Zhang, S. N., Song, H. F., Troyer, M. & Soluyanov, A. A. WannierTools: an open-source software package for novel topological materials. *Comput. Phys. Commun.* **224**, 405–416 (2018).